ChemComm

COMMUNICATION

View Article Online
View Journal | View Issue

Cite this: *Chem. Commun.*, 2022, 58, 1115

Received 9th November 2021,
Accepted 3rd December 2021

DOI: 10.1039/d1cc06314f

rsc.li/chemcomm

Reconstruction of bimetal $CoFe_{0.13}$-MOF to enhance the catalytic performance in the oxygen evolution reaction†

Kexin Yang,‡[a] Zeqi Jin,‡[a] Qicheng Zhang,[a] Qiming Chen,[a] Wenchao Peng,[ab] Yang Li,[ab] Fengbao Zhang,[ab] Qing Xia *[a] and Xiaobin Fan *[ab]

Oxygen evolution reaction (OER) is a key process in electrochemical energy conversion systems. This paper found that the solvothermal reconstruction could resume the original morphology and generate more oxygen vacancies on the surface of oxyhydroxide. The reconstructed electrocatalyst (re-$CoFe_{0.13}O_xH_y$) presents promising long-term stability (>85 h) under 1 M KOH condition without replacing the electrolyte.

Great efforts have been made towards the development of renewable energy to handle the energy crisis and environmental pollution. Electrocatalytic water splitting to produce hydrogen (H_2) and oxygen (O_2) is an ideal process for the large-scale production of clean and recyclable H_2. However, the oxygen evolution reaction (OER) represents one of the most critical steps as it involves a complicated four-electron-proton transfer. It plays an important role in the slower kinetics of the water splitting process, which makes the development of stable and efficient electrocatalysts for the OER a top priority.[1–3] Therefore, developing efficient electrocatalysts for the OER, especially the non-noble-metal electrocatalysts with high catalytic activity and stability, remains challenging.

The first-row transition metals, such as Ni, Co, and Fe, have attracted great attention, owing to their low cost and efficient electrocatalytic activities toward the OER. In particular, the transition metal-based metal organic frameworks (MOFs) are considered as promising OER electrocatalysts, because of their tunable porosity, large surface area and strong interfacial electronic coupling interactions.[4] However, during the water oxidation process, transition metal-based electrocatalyst surfaces always undergo reconstruction into high-valence metal sites such as oxyhydroxides and superoxides as active phases.[5–8] This *in situ* OER electrochemical reconstruction can also be referred to as the self-reconstruction process, which can cause changes in morphology and an increase or decrease in catalytic performance.[9,10] The rapid reconstruction not only makes electrocatalysts prone to peel off the electrode, resulting in severe structural corrosion and collapse after long-term OER processes, but also causes ripple effects such as lattice oxygen evolution, redeposition and amorphous surface formation.[11] Therefore, clearer understanding of the complex surface dynamic of the oxygen evolution electrode is in demand to design stable and efficient electrocatalysts.

Currently, some studies have improved the OER performance of transition metal-based OER electrocatalysts by modulating the reconstruction process.[12–14] For instance, Graves *et al.* demonstrated that severe electrolysis-induced degradation could be completely eliminated by a reversible shift between electrolysis and fuel-cell modes.[15] He *et al.* found that Na^+ dissolution enabled metal phosphides reconstruction to form defective oxyhydroxides as active catalytic sites.[16] Jiang *et al.* pointed out that phase transformation promoted by the etching of the lattice anion (Cl^-) could boost the OER activities.[17]

Despite this progress, it still remains a big challenge to develop a strategy to maintain the long-term stability of the catalysts during the OER process. This study brings forward a new strategy of multi-reconstructions to control the morphology and electronic structure of MOF-derived bimetal $CoFe_{0.13}$-MOF through different reconstruction processes. After two-step reconstructions, the final catalyst has more active (oxy)hydroxide and oxygen vacancies and shows extraordinary catalytic stability. It can maintain a current density of 10 mA cm^{-2} for more than 85 hours in 1 M KOH without changing the electrolyte.

With the molar ratio of Co to Fe adjusted to 1 : 0.13, the synthesis of the $CoFe_{0.13}$-MOF precursor was carried out in a Teflon-lined stainless-steel autoclave (please see details in the Experimental section). Then the $CoFe_{0.13}$-MOF was used as a pre-electrocatalyst for 50 000 s in 1 M KOH to obtain $CoFe_{0.13}O_xH_y$ through electrochemical oxidation at 10 mA cm^{-2}. The subsequent solvothermal reconstruction was carried out in an autoclave with

[a] *School of Chemical Engineering and Technology, State Key Laboratory of Chemical Engineering, Collaborative Innovation Center of Chemical Science and Engineering, Tianjin University, Tianjin 300072, People's Republic of China*
[b] *Chemistry and Chemical Engineering Guangdong Laboratory, Shantou, 515031, China. E-mail: xiaqing@tju.edu.cn, xiaobinfan@tju.edu.cn*

† Electronic supplementary information (ESI) available. See DOI: 10.1039/d1cc06314f

‡ These authors contributed equally.

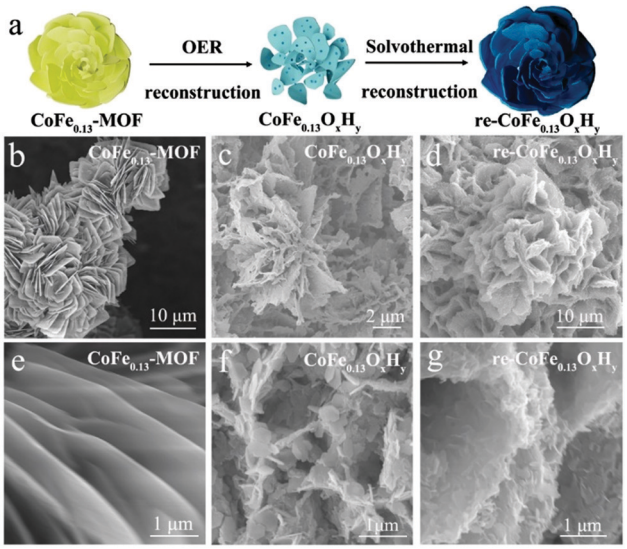

Fig. 1 (a) Schematic illustration of the fabrication process of the re-$CoFe_{0.13}O_xH_y$. SEM images of (b) $CoFe_{0.13}$-MOF, (c) $CoFe_{0.13}O_xH_y$, and (d) re-$CoFe_{0.13}O_xH_y$. (e)–(g) The enlarged images corresponding to (a)–(c).

DMF as the solvent at 100 °C for 15 h. Finally, the sample re-$CoFe_{0.13}O_xH_y$ was obtained as illustrated in Fig. 1a. The ratio of Co : Fe was about 11.6 : 1 in $CoFe_{0.13}$-MOF determined by the measurement of inductively coupled plasma mass spectrometry (ICP–EOS) (Table S1, ESI†). Note that the electronic structure of Co can be adjusted with a small amount of Fe to achieve better performance of the Co-based MOF.[18]

Note that nickel foam was used as a substrate, and it is impossible to get clear X-ray diffraction (XRD) patterns of the surface $CoFe_{0.13}$-MOF phase. However, the XRD pattern of the counterpart without the presence of nickel foam matches well with the simulated XRD pattern of $CoFe_{0.13}$-MOF in a previous study (Fig. S1, ESI†).[18,19] A weak diffraction peak at about $2\theta = 11.2°$, corresponding to the main diffraction of the $CoFe_{0.13}$-MOF was also identified. These results support the successful synthesis of $CoFe_{0.13}$-MOF on the nickel foam. After multiple reconstructions, the XRD peaks of the original $CoFe_{0.13}$-MOF disappear. The main peaks of the $CoFe_{0.13}O_xH_y$ and the re-$CoFe_{0.13}O_xH_y$ can be assigned to $Co(OH)_2$ (001) (JCPDS No. 30-0443) or CoOOH (003) (JCPDS No. 07-0169).[20] To study the changes of morphology, scanning electron microscopy (SEM) is employed. It is revealed that the original $CoFe_{0.13}$-MOF presents a micro-flower structure (Fig. 1b), which is formed by two-dimensional (2D) nanosheets with flat surfaces (Fig. 1e). After the OER reconstruction, as shown in Fig. 1c, the flower structure collapses, and the surface of these 2D nanosheets becomes corrosive and rough. The enlarged image shows that abundant sheet-like fragments with lateral sizes of less than 1 μm are clearly observed (Fig. 1f). Interestingly, the re-$CoFe_{0.13}O_xH_y$ after the final solvothermal reconstruction partially recovers the flower shape (Fig. 1d), and a hierarchical structure with the presence of smaller sheet-like fragments on the large nanosheets is clearly observed (Fig. 1g). Note that this hierarchical structure could render a larger surface area and the exposure of more catalytic active sites, which favor high electrocatalytic activity.

Transmission electron microscopy (TEM) reveals more detailed changes after the reconstruction processes. As shown in Fig. 2a, the $CoFe_{0.13}$-MOF nanosheets show clear edges and a layered structure, which are distinct from their counterparts after the reconstruction. In particular, the $CoFe_{0.13}O_xH_y$ is composited by abundant sheet-like fragments with hexagonal or irregular shapes (Fig. 2b). Broken edges or notches are clearly observed, resulting from the electrochemical oxidation during the OER. Similar results are also observed in the sheet-like fragments on the large nanosheets of the re-$CoFe_{0.13}O_xH_y$ (Fig. 2c) after the solvothermal reconstruction, but more topological defects and edges are present in the re-$CoFe_{0.13}O_xH_y$. The surface details of these fragments are seen in Fig. 2d. Given that no crystalline Fe species is detected by XRD, the lattice spacings of 0.258 and 0.230 nm correspond with pure and/or Fe-doped $Co(OH)_2$ (400)[21] and CoOOH (111) facets,[22–24] respectively.

As shown in the corresponding element mapping images (Fig. 2e), Co, Fe, Ni, C and O elements are uniformly distributed on the re-$CoFe_{0.13}O_xH_y$. The gradual increase of defects after the two reconstruction processes should significantly change the surface properties and provide more active sites for the OER.

To get further insights into the surface properties, we used X-ray photoelectron spectroscopy (XPS) to explore the valence state changes of the main catalytic elements in the $CoFe_{0.13}$-MOF before and after different reconstruction processes. The Co 2p XPS spectra of the primary and the reconstructed catalysts are given in Fig. 3a. The characteristic peaks of the Co 2p are identified as due to Co^{2+} species in the $CoFe_{0.13}$-MOF, which are located at the binding energies of 796.7 and 781.7 eV. Compared to the initial $CoFe_{0.13}$-MOF, the reconstructed $CoFe_{0.13}O_xH_y$ exhibits two new peaks centered at 795.1 and 780.2 eV, which are attributed to the Co^{3+} oxidation state. Meanwhile, the binding energies of Co^{2+} were shifted to 796.5 and 781.6 eV, suggesting an increase in the oxidation state of cobalt during the OER process.[25] Notably, the ratio of Co^{2+} to Co^{3+} in the re-$CoFe_{0.13}O_xH_y$ (0.94) is much larger than that in the $CoFe_{0.13}O_xH_y$ (0.46), indicating that a portion of Co^{3+} ions is reduced to Co^{2+} with generation of oxygen vacancies

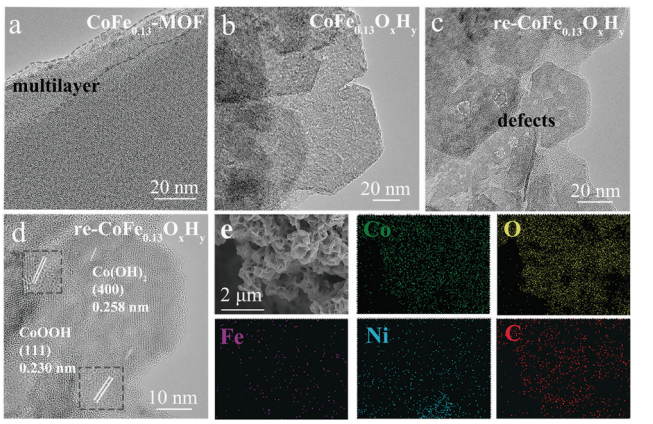

Fig. 2 TEM images of (a) $CoFe_{0.13}$-MOF, (b) $CoFe_{0.13}O_xH_y$, and (c) re-$CoFe_{0.13}O_xH_y$. (d) Enlarged image of the re-$CoFe_{0.13}O_xH_y$. Insets: Corresponding magnified lattice regions. (e) Corresponding EDX mapping images of the re-$CoFe_{0.13}O_xH_y$.

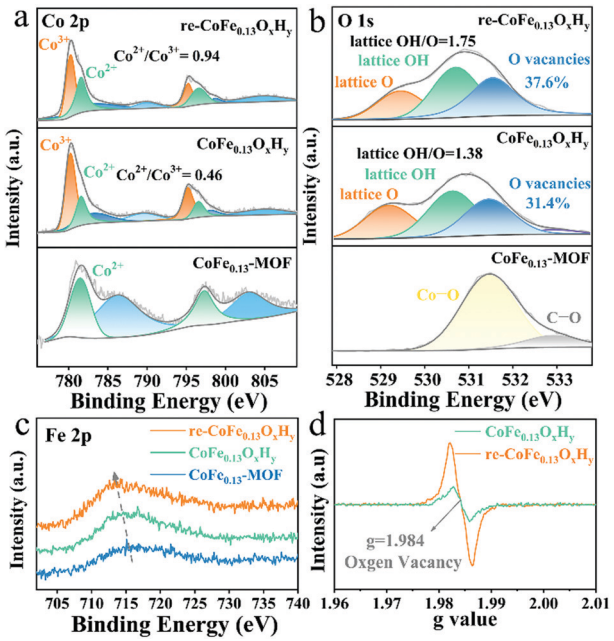

Fig. 3 XPS spectra of $CoFe_{0.13}$-MOF, $CoFe_{0.13}O_xH_y$ and re-$CoFe_{0.13}$-MOF. (a) Co 2p. (b) O 1s. (c) Fe 2p. (d) ESR spectra of $CoFe_{0.13}$-MOF and re-$CoFe_{0.13}$-MOF.

during the solvothermal reconstitution.[26] Attributed to the low surface Fe content (<1 at%; Table S2, ESI†), the signal-to-noise ratio of the Fe 2p spectra is poor, making it difficult to deconvolute into different chemical states. However, the overall trend clearly shows that compared with the re-$CoFe_{0.13}O_xH_y$, the Fe 2p (Fig. 3c) XPS of $CoFe_{0.13}$-MOF negatively shifts to a lower binding energy, which is consistent with the Co 2p XPS analyses.

At the same time, we observed obvious changes in the chemical state of the O element (Fig. 3b). In the primary $CoFe_{0.13}$-MOF, the O 1s spectrum shows two peaks located at 531.4 and 532.9 eV, corresponding to the Co–O and C–O bonds, respectively.[27] This result demonstrates that the metal and the organic ligands of the MOF are bound together by coordination.[28] After OER reconstruction, the O 1s spectrum of the $CoFe_{0.13}O_xH_y$ shows four peaks with binding energies of 529.19, 530.62, 531.45 and 532.90 eV, corresponding to lattice O, lattice OH, O vacancies and adsorbed O, respectively. As for the re-$CoFe_{0.13}O_xH_y$: there are three peaks at 529.45, 530.7 and 531.54 eV, attributed to lattice O, lattice OH and O vacancies, respectively.[29–31] Statistically, the lattice OH/O and O vacancies in re-$CoFe_{0.13}O_xH_y$ are obviously larger than those in $CoFe_{0.13}O_xH_y$, suggesting the fact that the OH/O rises and O vacancies grow after the second reconstruction. Furthermore, the electron spin resonance (ESR) measurements were employed to further verify the presence of O vacancies. As shown in Fig. 3d, the re-$CoFe_{0.13}O_xH_y$ shows higher paramagnetic signals than $CoFe_{0.13}O_xH_y$ at g = 1.984, which implies a high O-vacancies concentration.[32] The result agrees well with the XPS.[33] That is to say, the multiple reconstructions can increase the oxygen vacancies on the surface of the electrocatalyst.[34–36]

To probe the influence of the reconstruction processes on the performance of the $CoFe_{0.13}$-MOF, we measured linear sweep voltammetry (LSV) curves without iR-correction and the electrochemically active surface area (ECSA), to evaluate the electrocatalytic activities of all catalysts toward the OER. Fig. 4a compares the OER polarization curves of $CoFe_{0.13}$-MOF, $CoFe_{0.13}O_xH_y$ and re-$CoFe_{0.13}O_xH_y$ in a 1 M KOH solution. The LSV curves are collected at a scan rate of 5 mV s^{-1} after several cycles of cyclic voltammetry (CV) scans to minimize the capacitive current and reach a relatively stable state. The re-$CoFe_{0.13}O_xH_y$ displays an overpotential of 295 mV at a current density of 10 mA cm^{-2}, which is much lower than those of $CoFe_{0.13}O_xH_y$ (330 mV) and $CoFe_{0.13}$-MOF (319 mV), demonstrating that the OER performance is improved after reconstruction. Generally, the peak prior to the onset of the OER is related to the oxidation of Co(II) to Co(III) (CoOOH) that acts as the real active species for the OER.[37] The commercial RuO_2/C and Ni foam were also tested for comparison. As shown in Fig. S3 (ESI†), the overpotential of re-$CoFe_{0.13}O_xH_y$ at any current density is much lower than those of the commercial RuO_2 and the Ni foam, demonstrating the best electrocatalytic activity.

The Tafel plots in Fig. 4b also suggest the enhanced OER performance of re-$CoFe_{0.13}O_xH_y$. The drop in Tafel slope indicates that the oxygen evolution kinetics of re-$CoFe_{0.13}O_xH_y$ (71 mV dec^{-1}) are faster than those of $CoFe_{0.13}O_xH_y$ (125 mV dec^{-1}) and $CoFe_{0.13}$-MOF (108 mV dec^{-1}). The electrochemical double-layer capacitance (C_{dl}) measurements could indicate the ECSA of an electrocatalyst.[38] As shown in Fig. 4c, the re-$CoFe_{0.13}O_xH_y$, the $CoFe_{0.13}$-MOF and the $CoFe_{0.13}O_xH_y$ show C_{dl} values of 3.83, 3.21 and 1.83 μF cm^{-2}, respectively, illustrating that the multi-reconstruction process generates more active sites. The specific surface area (SSA) is measured *via* Brunauer–Emmett–Teller (BET) analysis of N_2 adsorption isotherms. Fig. S5 (ESI†) shows that the SSAs of $CoFe_{0.13}$-MOF, $CoFe_{0.13}O_xH_y$ and re-$CoFe_{0.13}O_xH_y$ are 3.16, 24.04 and 6.42 m^2 g^{-1}, respectively. Note that the restacking caused by the structural destruction caused a significant increase of ~4.54 nm mesopores on $CoFe_{0.13}O_xH_y$. However, the increase in SSA does not bring

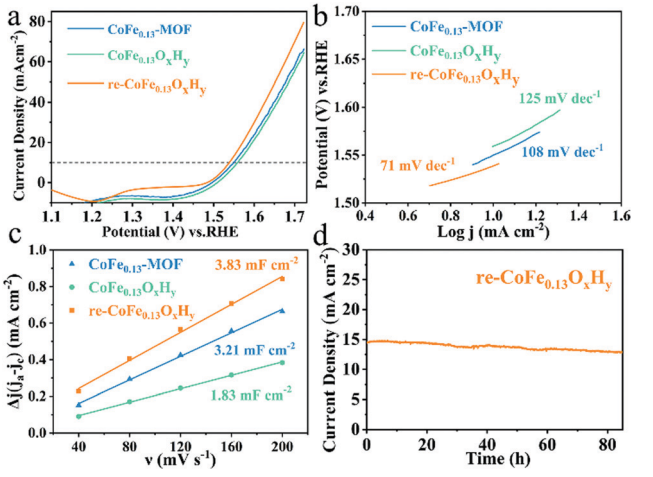

Fig. 4 Electrochemical characterization of the OER performance. (a) Polarization curves. (b) Tafel slopes. (c) C_{dl} calculations of $CoFe_{0.13}$-MOF, $CoFe_{0.13}O_xH_y$ and re-$CoFe_{0.13}O_xH_y$. (d) The stability test of the re-$CoFe_{0.13}O_xH_y$ catalyst during 85 h of OER reaction.

about an increase in catalytic activity. This confirms that the catalytic activity is positively correlated with the electrochemically active area, not the specific surface area. Electrochemical impedance spectroscopy (EIS) is also conducted to study the electrode kinetics in catalytic reactions. The Nyquist plots of re-$CoFe_{0.13}O_xH_y$, $CoFe_{0.13}O_xH_y$ and $CoFe_{0.13}$-MOF under the same potential are shown in Fig. S6 (ESI†). The plot of re-$CoFe_{0.13}O_xH_y$ suggests a smaller charge transfer resistance ($\sim$2.5 Ω) than those of $CoFe_{0.13}$-MOF ($\sim$4 Ω) and $CoFe_{0.13}O_xH_y$ ($\sim$4 Ω), implying the prior OER charge transfer kinetics of re-$CoFe_{0.13}O_xH_y$.[39] As for the catalytic stability test, the current density of the primary $CoFe_{0.13}$-MOF drops to 70% in less than 15 hours during oxygen evolution (Fig. S7, ESI†). The control sample with prolonged hydrothermal reaction time ($CoFe_{0.13}$-MOF-30 h) shows worse stability. After multi-reconstructions, however, re-$CoFe_{0.13}O_xH_y$ can work for over 85 hours at a current density of higher than 10 mA cm^{-2} with a 90% reserved current density (14.6 mA cm^{-2} to 13 mA cm^{-2}) (Fig. 4d). Compared with recently reported transition metal basic OER electrocatalysts (Table S3, ESI†), re-$CoFe_{0.13}O_xH_y$ exhibits outstanding stability at 10 mA cm^{-2}. All these results suggest that the catalytic performance of the original $CoFe_{0.13}$-MOF, especially the long-term stability, has been significantly improved by multi-reconstructions.

Subsequently, the reasons for its high stability were explained by analyzing the morphology, structure and elemental composition of the sample. As shown in Fig. S9 (ESI†), the second reconstruction of nano-flowers can stabilize the original morphology. There was no significant change in the morphology of the sample after 85 h of the OER process (re-$CoFe_{0.13}O_xH_y$-A). This can explain, at least in part, the fact that the current density in the stability test can remain undecayed for a long time. XRD patterns show that the re-$CoFe_{0.13}O_xH_y$-A is still amorphous after the stability test (Fig. S10, ESI†). XPS spectra of Co elements in re-$CoFe_{0.13}O_xH_y$-A (Fig. S12, ESI†) indicate that the ratio of Co^{2+} to Co^{3+} (0.77) was at a stable level, and no Co species are oxidized again. The highly consistent morphology, structure and elemental composition indicate that the secondary reconstruction enhances the stability of the material.

This study is supported by the National Natural Science Funds (No. 21878226, No. U20A20153), the Chemistry and Chemical Engineering Guangdong Laboratory (Grant No. 1912011).

Conflicts of interest

There are no conflicts to declare.

Notes and references

1 X. Z. Song, N. Zhang, X. F. Wang and Z. Tan, *Mater. Today Energy*, 2021, **19**, 100597.
2 Y. Li, F. M. Li, X. Y. Meng, S. N. Li, J. H. Zeng and Y. Chen, *ACS Catal.*, 2018, **8**, 1913–1920.
3 L. G. Li, P. T. Wang, Q. Shao and X. Q. Huang, *Chem. Soc. Rev.*, 2020, **49**, 3072–3106.
4 Z. Q. Li, R. Gao, M. Feng, Y. P. Deng, D. Wang, Q. Li, H. B. Li, X. Wang and Z. W. Chen, *Adv. Energy Mater.*, 2021, **11**, 27.
5 J. Zhou, Y. Wang, X. Su, S. Gu, R. Liu, Y. Huang, S. Yan, J. Li and S. Zhang, *Energy Environ. Sci.*, 2019, **12**, 739–746.
6 S. Zhang, T. Yu, H. Wen, Z. Ni, Y. He, R. Guo, J. You and X. Liu, *Chem. Commun.*, 2020, **56**, 15387–15405.
7 J. Tian, F. Jiang, D. Yuan, L. Zhang, Q. Chen and M. Hong, *Angew. Chem., Int. Ed.*, 2020, **59**, 13101–13108.
8 A. Moysiadou, S. Lee, C. S. Hsu, H. M. Chen and X. Hu, *J. Am. Chem. Soc.*, 2020, **142**, 11901–11914.
9 K. Xu, H. Cheng, L. Q. Liu, H. F. Lv, X. J. Wu, C. Z. Wu and Y. Xie, *Nano Lett.*, 2017, **17**, 578–583.
10 S. Z. Song, J. Zhou, X. Z. Su, Y. Wang, J. Li, S. Zhang and J. Q. Wang, *Energy Environ. Sci.*, 2018, **11**, 2945–2953.
11 C. Kuai, Z. Xu, C. Xi, A. Hu, Z. Yang, Y. Zhang, C.-J. Sun, L. Li, D. Sokaras, X.-W. Du and F. Lin, *Nat. Catal.*, 2020, **3**, 743–753.
12 H. Jiang, Q. He, Y. Zhang and L. Song, *Acc. Chem. Res.*, 2018, **51**, 2968–2977.
13 T. Wu, S. Sun, J. Song, S. Xi, Y. Du, L. Zeng, H. Wang, H. Li, A. Grimaud and Z. J. Xu, *Nat. Catal*, 2019, **2**, 763–772.
14 A. Mavrič, M. Fanetti, Y. Lin, M. Valant and C. Cui, *ACS Catal.*, 2020, **10**, 9451–9457.
15 C. Graves, S. D. Ebbesen, S. H. Jensen, S. B. Simonsen and M. B. Mogensen, *Nat. Mater.*, 2015, **14**, 239–244.
16 Q. He, H. Xie, Z. U. Rehman, C. Wang, P. Wan, H. Jiang, W. Chu and L. Song, *ACS Energy Lett.*, 2018, **3**, 861–868.
17 H. Jiang, Q. He, X. Li, X. Su, Y. Zhang, S. Chen, P. M. Ajayan and L. Song, *Adv. Mater.*, 2019, **31**, 1805127.
18 Z. Q. Xue, K. Liu, Q. L. Liu, Y. L. Li, M. Liu and G. Q. Li, *Nat. Commun.*, 2019, **10**, 8.
19 Z.-L. Huang, M. Drillon, N. Masciocchi, A. Sironi, J.-T. Zhao, P. Rabu and P. Panissod, *Chem. Mater.*, 2000, **12**, 2805–2812.
20 W. Zheng, M. Liu and L. Y. S. Lee, *ACS Catal.*, 2020, **10**, 81–92.
21 S. Wan, J. Qi, W. Zhang, W. Wang, S. Zhang, K. Liu, H. Zheng, J. Sun, S. Wang and R. Cao, *Adv. Mater.*, 2017, **29**, 1702724.
22 W. Zhao, C. Peng, Z. Kuang, Q. Zhang, Y. Xue, Z. Li, X. Zhou and H. Chen, *Chem. Eng. J.*, 2020, **398**, 125537.
23 J. Hu, S. W. Li, J. Y. Chu, S. Q. Niu, J. Wang, Y. C. Du, Z. H. Li, X. J. Han and P. Xu, *ACS Catal.*, 2019, **9**, 10705–10711.
24 J. X. Feng, H. Xu, Y. T. Dong, S. H. Ye, Y. X. Tong and G. R. Li, *Angew. Chem., Int. Ed.*, 2016, **55**, 3694–3698.
25 Y. Yan, K. Bao, T. Liu and J. Qi, *Chem. Eng. J.*, 2020, **401**, 126092.
26 Q. Hu, X. Huang, Z. Wang, G. Li, Z. Han, H. Yang, P. Liao, X. Ren, Q. Zhang, J. Liu and C. He, *Small*, 2020, **16**, e2002210.
27 R. Xu, Q. Ji, P. Zhao, M. Jian, C. Xiang, C. Hu and J. Qu, *J. Mater. Chem. A*, 2020, **8**, 7870–7879.
28 Q. J. Ji, J. X. Xu, C. Wang and L. Wang, *J. Colloid Interface Sci.*, 2021, **596**, 139–147.
29 M. Kuang, J. Zhang, D. Liu, C. Liu, L. Song, B. Liu and Q. Yan, *Adv. Energy Mater.*, 2020, **10**, 2002215.
30 C. Meng, M. Lin, X. Sun, X. Chen, X. Chen, X. Du and Y. Zhou, *Chem. Commun.*, 2019, **55**, 2904–2907.
31 Z.-F. Huang, J. Song, Y. Du, S. Xi, S. Dou, J. M. V. Nsanzimana, C. Wang, Z. J. Xu and X. Wang, *Nat. Energy*, 2019, **4**, 329–338.
32 Y. Su, J. Lang, L. Li, K. Guan, C. Du, L. Peng, D. Han and X. Wang, *J. Am. Chem. Soc.*, 2013, **135**, 11433–11436.
33 Y. Fu, L. Li, S. Ye, P. Yang, P. Liao, X. Ren and C. He, *J. Mater. Chem. A*, 2021, DOI: 10.1039/d0ta10389f.
34 M. Asnavandi, Y. Yin, Y. Li, C. Sun and C. Zhao, *ACS Energy Lett.*, 2018, **3**, 1515–1520.
35 J. Wang, J. Liu, B. Zhang, F. Cheng, Y. Ruan, X. Ji, K. Xu, C. Chen, L. Miao and J. Jiang, *Nano Energy*, 2018, **53**, 144–151.
36 W. Sevenhans, M. Gijs, Y. Bruynseraede, H. Homma and I. K. Schuller, *Phys. Rev. B: Condens. Matter Mater. Phys.*, 1986, **34**, 5955–5958.
37 Z. W. Gao, J. Y. Liu, X. M. Chen, X. L. Zheng and J. Mao, *Adv. Mater.*, 2019, **31**, e1804769.
38 Z. Lu, L. Qian, Y. Tian, Y. Li, X. Sun and X. Duan, *Chem. Commun.*, 2016, **52**, 908–911.
39 Q. M. Chen, Q. C. Zhang, H. B. Liu, J. M. Liang, W. C. Peng, Y. Li, F. B. Zhang and X. B. Fan, *Small*, 2021, **17**(13), 2007858.

